nature physics

Article

https://doi.org/10.1038/s41567-025-03140-z

Emergent signatures of the glass transition in colloidal suspensions

Received: 22 August 2024

Accepted: 19 November 2025

Patrick Laermann [1], Haim Diamant [2,3], Yael Roichman [2,3,4], Ivo Buttinoni [5], Manuel A. Escobedo-Sánchez [1] ✉ & Stefan U. Egelhaaf [1]

At the glass transition, a liquid transforms into an amorphous solid. Despite minimal structural rearrangements, this transition is accompanied by a dramatic dynamical slowdown. These features render the transition's experimental determination and theoretical understanding challenging. Here we introduce a new framework that uses two-particle correlations and a model-free theoretical description to investigate the dynamics of glass-forming colloidal suspensions indirectly. Using the fluctuation-dissipation theorem, we relate equilibrium thermal fluctuations of pairs of tracer particles to the underlying response properties of the system. We measure the correlated motion of tracer particles caused by the solvent at short timescales and find three distinct signatures signalling the onset of the glass transition. The correlations in the thermal motions of tracer pairs exhibit a changing decay behaviour with their relative distance; a length scale related to this decay steeply increases; and a notable sign reversal is observed in specific correlations. Our findings establish a connection between the colloidal glass transition and the breaking of the translational symmetry in the dispersion medium, thereby revealing fundamental aspects of the glass transitions.

How does a liquid transform into a glass[1,2]? When examining the glass transition, two fundamental questions arise in comparison with classical phase transitions: Does the relaxation time τ_r truly diverge at a critical temperature or density, and is this divergence associated with an emergent increasing length scale? Moreover, does the transition involve symmetry breaking, making the glass a distinct state of matter, even if not necessarily an equilibrium state? Concerning the relaxation time (τ_r), there is a general consensus that it effectively diverges, supported by experimental and computational evidence showing that it increases dramatically near the glass transition, fitting well with divergent functions[1,2]. However, evidence for a diverging length scale remains less definitive. Although increasingly large domains of cooperatively moving particles ('dynamic heterogeneities') are observed near the transition[1], their growth remains modest, typically limited to a few particle diameters[1,3,4]. Regarding symmetry breaking, several studies suggest a critical behaviour and subtle symmetry breaking at the glass transition[5,6]. A widely accepted and predictive theory[6] strongly supports the notion that the glass transition is a critical phenomenon associated with symmetry breaking and a divergent correlation length. Yet, this mean-field theory is exact only in high dimensions, and it remains uncertain whether the predicted critical behaviour persists or is substantially altered in three-dimensional (3D) systems[7]. This unresolved issue has practical implications for various applications utilizing synthetic glassy materials composed of atoms, molecules, polymers, colloids or granular particles[8,9]. The challenge extends to biological systems, where glassy behaviour can elucidate the dynamics and reorganization processes in individual cells[10,11] and tissues[12–19].

Among all glassy materials, those prepared using colloidal suspensions offer remarkable advantages[20–23]. They contain nanometre- to micrometre-sized particles that undergo thermal fluctuations

---

[1]Condensed Matter Physics Laboratory, Heinrich Heine University, Düsseldorf, Germany. [2]School of Chemistry, Tel Aviv University, Tel Aviv, Israel. [3]Center for Physics and Chemistry of Living Systems, Tel Aviv University, Tel Aviv, Israel. [4]School of Physics and Astronomy, Tel Aviv University, Tel Aviv, Israel. [5]Institute of Experimental Colloidal Physics, Heinrich Heine University, Düsseldorf, Germany. ✉e-mail: escobedo@hhu.de

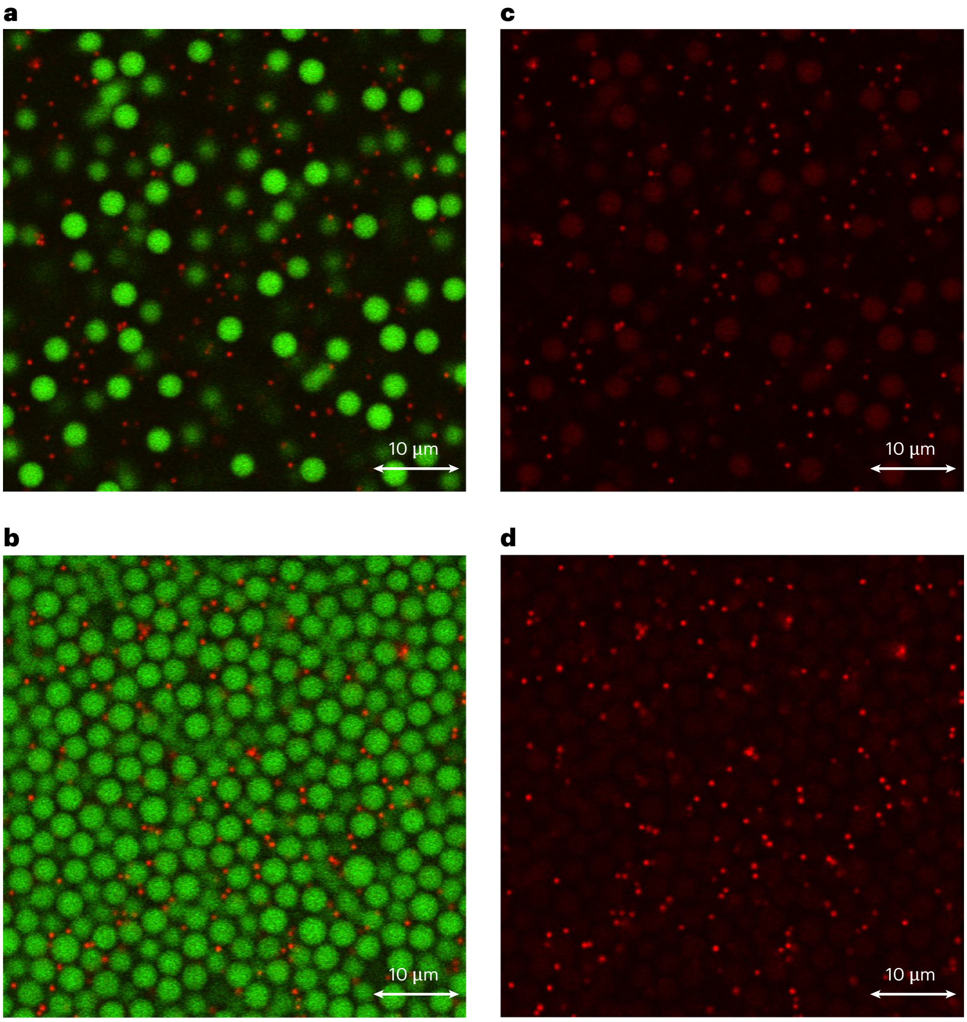

Fig. 1 | Representative images of the bi-disperse colloidal suspension. **a**,**b**, Two-channel confocal microscopy images of a suspension containing large particles (green) and small tracer particles (red) are shown for [$\phi = 0.15$, $\phi_s = 0.0050$] (**a**) and [$\phi = 0.58$, $\phi_s = 0.0058$] (**b**). **c**,**d**, The corresponding one-channel images of the tracer particles, acquired simultaneously with the two-channel images.

(like atoms and molecules) in a dispersion medium and can be individually resolved using optical microscopy (unlike atoms and molecules)[20]. In particular, colloidal particles with hard-sphere-like interactions have attracted widespread interest[22–25] because their suspension's thermodynamic state is controlled solely by the volume fraction of the particles, ϕ. In equilibrium, hard spheres crystallize above $\phi \approx 0.545$, but size polydispersity or small stresses can suppress crystallization and allow the fluid phase to remain supercooled up to $\phi \approx 0.58$, beyond which it is commonly thought to solidify into a glass[20,22]. In recent decades, studies of colloidal supercooled liquids and glasses have shed light on many fundamental problems, including non-Newtonian flow, jamming and ageing[20]. Although the structure of colloidal glasses is more accessible than that of atomic amorphous materials, studying the dynamics near the glass transition remains extremely challenging due to the dramatic slowdown in the particle motion. To avoid this issue, a small fraction of notably smaller particles can be added to the suspension[26–28]. These tracers remain mobile even when the matrix solidifies, explore the structural voids and are carried by any large-scale flow generated by the surrounding medium. Their motion can be tracked directly using optical microscopy or indirectly by means of light scattering and scattering-like techniques such as differential dynamic microscopy (DDM)[26–31]. In particular, at timescales sufficiently large for the tracers to explore the voids, self- and collective diffusion quantities shed light on the matrix mobility even in the absence of an explicit solvent[26]. Although DDM provides access to the self-intermediate scattering function for tracer particles or the total intermediate scattering function in concentrated systems, the two-point correlation analysis directly resolves spatial cross-correlations in real space, explicitly capturing the pairwise mobility tensor[32].

In this Article, we introduce an alternative framework that examines tracer dynamics on much shorter timescales, allowing thermal motion to reflect large-scale flow properties of the solvent through the fluctuation-dissipation theorem. Because these flow properties are affected by the collective motion of the glass-forming suspension, our model-free theoretical analysis reveals previously unidentified signatures of the glass transition. In particular, two-point correlation functions between the displacements of the tracers separated by a distance r (1) show different spatial decay patterns, (2) undergo a sign inversion and (3) result in a characteristic length scale that is bound to diverge with the square root of the viscosity of the suspension.

Experiments

The glass-forming suspensions are composed of polymethylmethacrylate (PMMA) particles with diameter $2a_l = 3.19$ µm and polydispersity $\delta_l \approx 7\%$ that are fluorescently labelled using monomerized 4-methyl-aminoethylmethacrylate-7-nitro-benzo-2-oxal,3-diazol (NBD).

The particles are suspended in an index- and density-matched mixture of *cis*-decalin and cycloheptylbromide that prevents particle sedimentation and turbidity. In addition, the suspension behaves as a hard-sphere-like system[23,25,33], where interactions between particles occur only upon contact. The investigated range of volume fractions, $0.05 \le \phi \le 0.60$, includes liquid and supercooled phases. Notably smaller PMMA particles, with diameter $2a_s = 0.50\ \mu\text{m}$, polydispersity $\delta_s \approx 7\%$, monomerized rhodamine B as fluorescent label and volume fraction $\phi_s \approx 0.005$, are added as tracers. Representative confocal images of the binary mixture are shown in Fig. 1; the matrix particles and tracers appear green and red, respectively. Using a two-channel confocal microscopy set-up, we independently imaged the differently dyed particle species, as simultaneous acquisition causes signal leakage between them (Fig. 1c,d). Therefore, for our measurements, we used only one laser and one channel per acquisition. This approach ensures stable image quality and enables clear, accurate visualization of the tracer particles. As the volume fraction of large particles increases (from Fig. 1a,b and from Fig. 1c,d), the tracers start to occupy the voids of the dense structure. A detailed description of the experimental realization and data analysis is available in the Supplementary Information.

An optical section of ~0.4 µm was used without performing a 3D scan, making both the measurements and the analysis two-dimensional while probing bulk properties. We characterize the dynamics of the system by extracting the trajectories $\mathbf{R}_i(t)$ and $\mathbf{r}_j(t)$ of each large and small particle. The corresponding mean squared displacements averaged over all particles are shown in Fig. 2a ($\mathrm{MSD}_{\Delta R}(\tau)$, large particles) and Fig. 2b ($\mathrm{MSD}_{\Delta r}(\tau)$, tracers) for increasing volume fraction of the matrix. At $\phi \ge 0.57$, $\mathrm{MSD}_{\Delta R}(\tau)$ hardly increases with time, confirming the arrest of particle motion and thus reproducing the previously reported colloidal glass transition of hard-sphere suspensions[20,22]. By contrast, the tracer particles stay mobile up to about 10 Brownian times ($\tau_s^B = 3\pi\eta_0(2a_s)^3/k_BT \approx 1\ \text{s}$) even for very high volume fractions, before they start to become sensitive to the finite cages of the structure. In this work, we focus on the dynamics during delay time $\tau = 68\ \text{ms} \approx 0.07\tau_s^B$ (Fig. 2b, inset), over which each particle is able to explore only the area schematically indicated by the dashed circles in Fig. 2c. Thus, the large particles hardly move (compared with their size), whereas the small particles exhibit diffusive behaviour. Any anomalous dynamics, for example due to caging effects, occur on much larger timescales ($\tau > 1$ s), and the motion of the tracers is determined solely by Brownian motion or by large-scale fluid flows induced by the mobility of the matrix.

To gain insight into the glass transition of the suspension, we consider all pairs of tracers, i and j, separated by a distance $r(t) = |\mathbf{r}(t)| = |\mathbf{r}_j(t) - \mathbf{r}_i(t)|$ and extract the displacements of the two tracers along their connecting line ($\Delta x_i(t,\tau) = \Delta\mathbf{r}_i(t,\tau)\cdot\mathbf{r}(t)/r(t)$) and perpendicular to it ($\Delta y_i(t,\tau)$) (and correspondingly $\Delta x_j(t,\tau)$ and $\Delta y_j(t,\tau)$) (see sketch in Fig. 2d). Finally, the longitudinal, $D_\parallel(r,\tau)$, and transversal, $D_\perp(r,\tau)$, two-point correlation functions are obtained as

$$\begin{aligned} D_\parallel(r,\tau) &= \langle \Delta x_i(t,\tau)\Delta x_j(t,\tau)\rangle_{(i,j)_{r(t)},t}, \\ D_\perp(r,\tau) &= \langle \Delta y_i(t,\tau)\Delta y_j(t,\tau)\rangle_{(i,j)_{r(t)},t}. \end{aligned} \qquad (1)$$

The angular brackets $\langle\cdots\rangle_{(i,j)_{r(t)},t}$ denote an average over all pairs i and j separated by the same distance $r(t)$ for all starting times t. $D_\parallel$ and $D_\perp$ quantify the degree to which the random thermal motions of the two tracers are correlated along and perpendicular to their connecting line, respectively. The longitudinal and transversal correlations are illustrated for a liquid suspension ($\phi = 0.05$) and a supercooled one ($\phi = 0.59$) in Fig. 2e. Substantial correlations between the tracers are observed in the liquid state, whereas the correlations are weaker but measurable in the supercooled suspension. The decay as a function of the relative distance r is also qualitatively different in the two cases (Fig. 2e, inset).

The pronounced increase in correlations for $D_\parallel$ at separations $r \lesssim 1\ \mu\text{m}$ (Fig. 2e) originates from the local structure of tracers, as captured by the radial distribution function (Supplementary Fig. 27) and is consistent with previous findings for quasi-two-dimensional concentrated systems[34]. This increase is also observed in computer simulations in the absence of hydrodynamic interactions (Supplementary Information), further verifying that it results purely from the structural arrangements. We have excluded this short-distance region from the main analysis.

This strategy of analysing pairwise correlated displacements as a function of interparticle distance forms the basis of two-point microrheology, a powerful technique used to probe the elastic and viscous moduli of complex materials[32]. In purely viscous fluids, the mobility matrix becomes time independent, the two-point correlation functions increase linearly with τ and the method reveals how the strain-rate field decays through the fluid[35].

Our framework belongs to this purely viscous category, because over $\tau = 68$ ms the tracers interact solely with the surrounding fluid. However, they still sense the matrix indirectly via its effect on the fluid flow. Without solvent, at $\tau = 68$ ms, $D_\parallel(r,\tau)$ and $D_\perp(r,\tau)$ of equation (1) would vanish (Supplementary Fig. 30d). Figure 3 displays the two-point correlations as functions of τ for various volume fractions ϕ and particle separations r. The linearity observed around the relevant delay time ($\tau \approx 68$ ms) confirms that the medium behaves predominantly as a viscous liquid within this time regime; thus, elasticity can be precluded. This is further supported by the linear dependence on τ of the one-point $\mathrm{MSD}_{\Delta r}(\tau)$ in the same time range (Fig. 2b).

We now focus on the r dependence of $D_\parallel(r,\tau)$ and $D_\perp(r,\tau)$ at $\tau = 68$ ms to find distinct signatures. Figure 4 presents the two-point correlations $D_\parallel(r,\tau)$ and $D_\perp(r,\tau)$ for various volume fractions ϕ. In the longitudinal direction (Fig. 4a), the correlations decay monotonically for $r \gtrsim 1\ \mu\text{m}$, with the decay rate strongly dependent on the volume fraction. For dilute suspensions (low ϕ), the decay follows $D_\parallel(r,\tau) \propto r^{-1}$ and is consistent with long-range hydrodynamic interactions in Newtonian fluids. By contrast, at higher-volume fractions (supercooled states), the decay becomes notably steeper, approaching r^{-3}, which reflects the suppression of fluid propagation due to the dense matrix. The transverse correlations $D_\perp(r,\tau)$ (Fig. 4b,c) exhibit two additional features. First, for $\phi > 0.45$, $D_\perp(r,\tau)$ shows a non-monotonic dependence on r, and for the highest densities it becomes negative at small separations, indicating anticorrelated motion between nearby tracers, a signature of mechanical constraints in solid environments[36,37]. Second, in the liquid state, the amplitude of $D_\perp(r,\tau)$ is approximately half that of $D_\parallel(r,\tau)$ (Supplementary Fig. 24), in agreement with theoretical expectations for isotropic hydrodynamic coupling[38]. To disentangle these spatial effects caused by the matrix from changes in single-tracer mobility, we normalize both $D_\parallel(r,\tau)$ and $D_\perp(r,\tau)$ by the ϕ-dependent mean squared displacement $\mathrm{MSD}_{\Delta r}(\tau = 68\ \text{ms})$ (Fig. 2b, inset). The resulting curves (Fig. 4d–f) retain their distinct r dependence, confirming that the observed changes in the correlations arise from hydrodynamic interactions. This normalization removes the trivial scaling $\mathrm{MSD} \propto \tau$ and isolates the spatial dependence encoded in the pair-coupling mobility tensors that enter equation (1).

To gain a quantitative understanding of the correlations as a function of ϕ and r, we fitted the decaying part of the logarithm of the longitudinal data to a linear equation with slope $-\alpha$, that is $D_\parallel(r,\tau) \propto r^{-\alpha}$, over varying intervals of separations r (Fig. 5a). This resolves the spatial crossover between the two power-law decays at different values of ϕ. For $1.3\ \mu\text{m} \le r \le 1.8\ \mu\text{m}$, α as a function of ϕ gradually changes from $\alpha \approx 1$ at low ϕ to a value around $\alpha \approx 3$ for the supercooled suspensions. Thus, the dynamical slowdown of the large particles is reflected in the dynamics of the tracers, which, however, are never arrested (Fig. 2b). For larger separation intervals, the increase in α begins at a higher value of ϕ and becomes sharper. Motivated by these results and the model described below (equation (9a)), we fit the longitudinal data to a

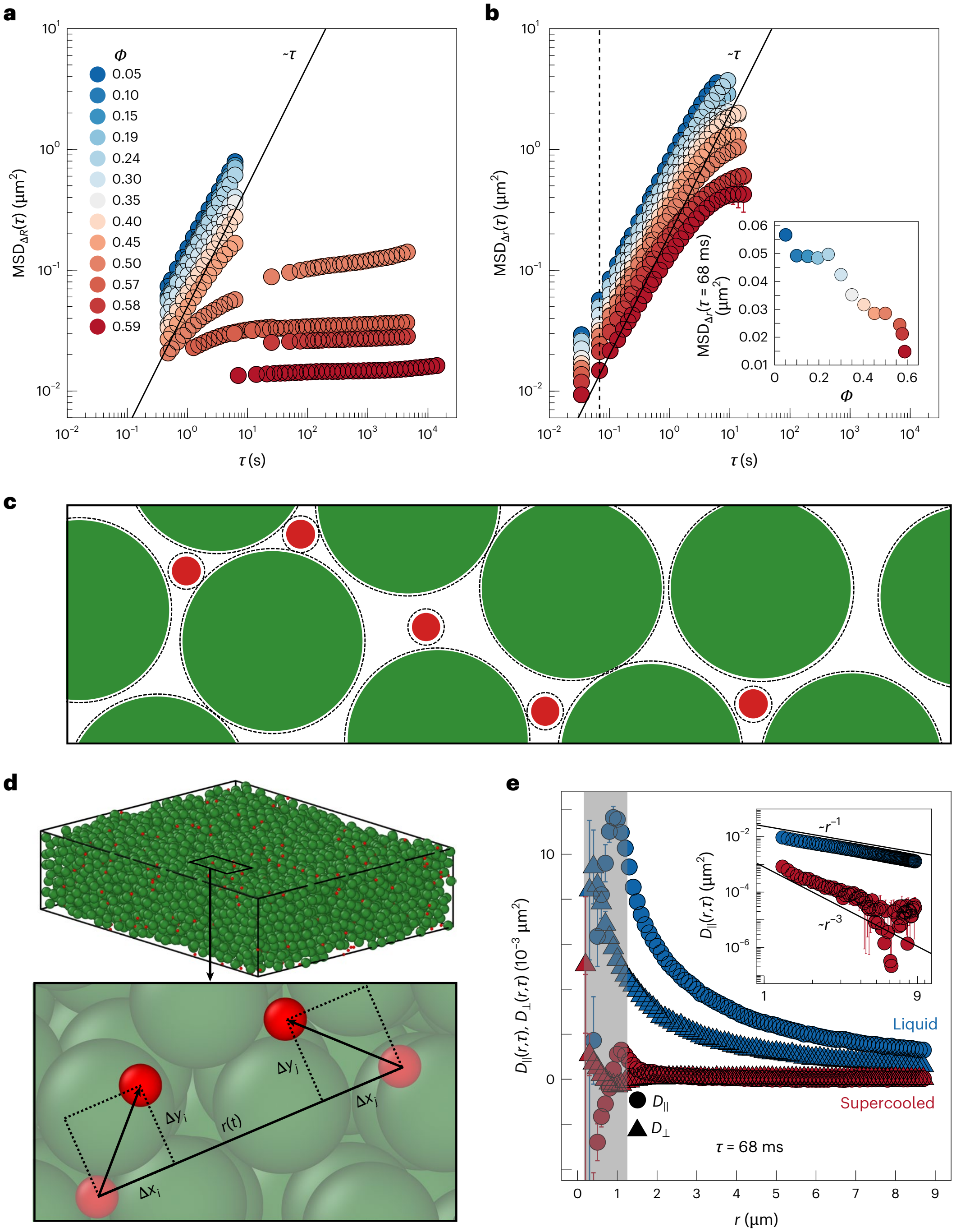

Fig. 2 | Overview of particle dynamics from the bi-disperse colloidal suspension's one- and two-point observables. One-point dynamics of large and tracer particles across the glass transition. **a**, Mean squared displacement MSD$_{\Delta R}(\tau)$ of large particles as a function of delay time τ, for various volume fractions ϕ. **b**, MSD$_{\Delta r}(\tau)$ of tracer particles for the same volume fractions. The vertical dashed line indicates $\tau = 68$ ms. The inset shows MSD$_{\Delta r}(\tau = 68$ ms). **c**, Schematic cross-section illustrating, to scale, the spatial positioning of tracer (red) and large (green) particles for a suspension of $\phi = 0.5$. Tracer particles primarily reside in the voids formed between the larger particles. The dashed circles indicate the regions each particle is able to explore during the chosen time interval $\tau = 68$ ms. **d**, A 3D visualization of the system and the method for measuring two-point correlations between well-separated tracers at distance $r(t)$. **e**, Flow-mediated two-point displacement correlations $D_{\|}(r,\tau)$ and $D_{\perp}(r,\tau)$ for liquid (blue) and supercooled (red) states at $\tau = 68$ ms. The data in **a** and **e** represent the weighted mean from N_{area} (≥10) different areas (technical replicates), where N_{area} varied for each ϕ (Supplementary Table 3). The error bars represent the corresponding weighted s.d. The weighting is based on the number of displacements (one-point or two-point) and is applied consistently to both the mean and s.d. calculation. The error bars may be smaller than the symbol size.

superposition of the two power laws, $D_{\|} = 2A_{\|}(r^{-1} + \ell^2 r^{-3})$. The coefficient $A_{\|}$, which determines the overall strength of the correlation, is expected to be inversely proportional to the viscosity of the suspension η. The coefficient ℓ^2, in units of length squared, defines a crossover separation length ℓ before and after which the correlations are dominated by the r^{-3} or r^{-1} term, respectively. Figure 5b shows the dependence of ℓ^2 on ϕ, exhibiting a steep increase for the supercooled suspensions. The extraction of α and ℓ from the transversal correlation $D_{\perp}$ is consistent with the analysis above but statistically more challenging due to the non-monotonic behaviour of this correlation.

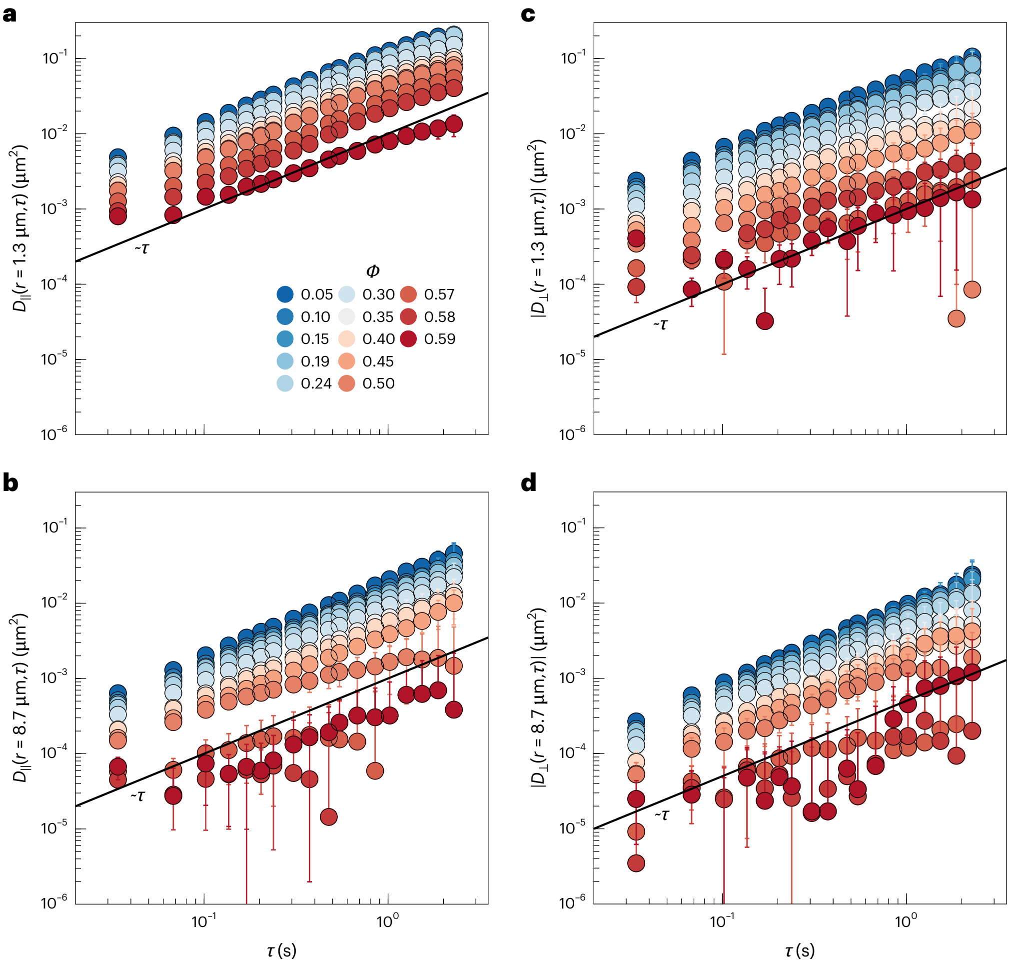

Fig. 3 | Time dependence of the two-point correlation functions. **a**–**d**, Longitudinal $D_{\parallel}(r,\tau)$ (**a** and **b**) and transversal $|D_{\perp}(r,\tau)|$ (**c** and **d**) as functions of delay time τ for different volume fractions ϕ, shown for $r = 1.3$ μm (**a** and **c**) and $r = 8.7$ μm (**b** and **d**). These distances represent the lower and upper bounds of the r regions analysed in this work. Solid lines indicate a linear increase with τ. The data in **a**–**d** represent the weighted mean from N_{area} (≥10) different areas (technical replicates), where N_{area} varied for each ϕ (Supplementary Table 3). The error bars represent the corresponding weighted s.d. The weighting is based on the number of two-point displacements and is applied consistently to both the mean and s.d. calculation. The error bars may be smaller than the symbol size.

Theory

The experimental results are now rationalized using a model-free approach based on conservation laws[36,37]. A more elaborate analysis is found in ref. 39.

We start by considering the overdamped stochastic dynamics of a pair of tracer particles in a fluid. The dynamics are described by an overdamped Langevin equation[40,41],

$$\frac{\mathrm{d}}{\mathrm{d}t} r_{i,\vartheta}(t_0) = M_{ij,\vartheta\beta}(\mathbf{r}_1(t_0), \mathbf{r}_2(t_0)) \left[F_{j,\beta}(t_0) + \xi_{j,\beta}(t_0) \right], \tag{2}$$

where $i, j = (1, 2)$ label the particles and $\vartheta, \beta = (x, y, z)$ denote Cartesian coordinates. Summation over repeated indices is implied. The position vector of particle i at time t has the component $r_{i,\vartheta}(t)$ in the ϑ direction; $F_{i,\vartheta}$ and $\xi_{i,\vartheta}$ are the ϑ-components of the deterministic and random forces acting on particle i, respectively. (We have omitted the 'spurious drift' term appearing in the formulation[40] because, in the approximation to follow, the mobility matrix $M_{ij,\vartheta\beta}$ is divergence-free.) The pair-mobility matrix $M_{ij,\vartheta\beta}$ depends on the instantaneous spatial configuration of the pair, $(\mathbf{r}_1(t), \mathbf{r}_2(t))$. The matrix contains self-mobility blocks ($i = j$), which relate the velocity of each particle to the force acting on itself, and coupling-mobility blocks ($i \neq j$), which relate the velocity of each particle to the force acting on the other (that is, the hydrodynamic interaction between the two). For a purely viscous medium (which is the case in our measurements), the mobility matrix does not have an explicit dependence on time. The dispersion medium is at equilibrium and therefore satisfies the fluctuation-dissipation theorem, which dictates

$$\langle \xi_{i,\vartheta}(t) \rangle = 0, \quad \langle \xi_{i,\vartheta}(t) \xi_{j,\beta}(t') \rangle = 2 k_{\mathrm{B}} T (M^{-1})_{ij,\vartheta\beta}\, \delta(t - t'). \tag{3}$$

Our measurements are taken over a short time interval τ such that the configuration $(\mathbf{r}_1, \mathbf{r}_2)$ remains effectively unchanged (Fig. 2c). In addition, our tracers are force-free, $\mathbf{F}_i = 0$. Integration of equation (2) while using equation (3) gives the displacement correlations,

$$\langle \Delta r_{i,\vartheta}(t_0, \tau) \Delta r_{j,\beta}(t_0, \tau) \rangle = 2 k_{\mathrm{B}} T \tau M_{ij,\vartheta\beta}(\mathbf{r}_1(t_0), \mathbf{r}_2(t_0)), \tag{4}$$

which relates the measured two-point displacement correlations, equation (1), to the coupling blocks of the mobility matrix. In the limit where the tracers' size is much smaller than their separation, $a_{\mathrm{s}} \ll r \equiv |\mathbf{r}_2 - \mathbf{r}_1|$, the coupling mobility becomes independent of the particles' properties and equal to the flow velocity response $(G_{\vartheta\beta}(\mathbf{r}))$ to a point force, $M_{i\neq j,\vartheta\beta}(\mathbf{r}_1, \mathbf{r}_2) \approx G_{\vartheta\beta}(\mathbf{r})$. This 'stokeslet approximation'[42] is similar to the monopole–monopole limit of the electrostatic interaction between charged particles at large separations (large-separation limit), given simply by the Coulomb potential. Thus, the coupling mobility reflects the properties of the surrounding medium on a large-scale r. (This is the basis of two-point microrheology[32].) Defining the x axis along the separation vector, $\mathbf{r} = r\hat{\mathbf{x}}$, equation (4) simplifies in the large-separation limit to

https://doi.org/10.1038/s41567-025-03140-z

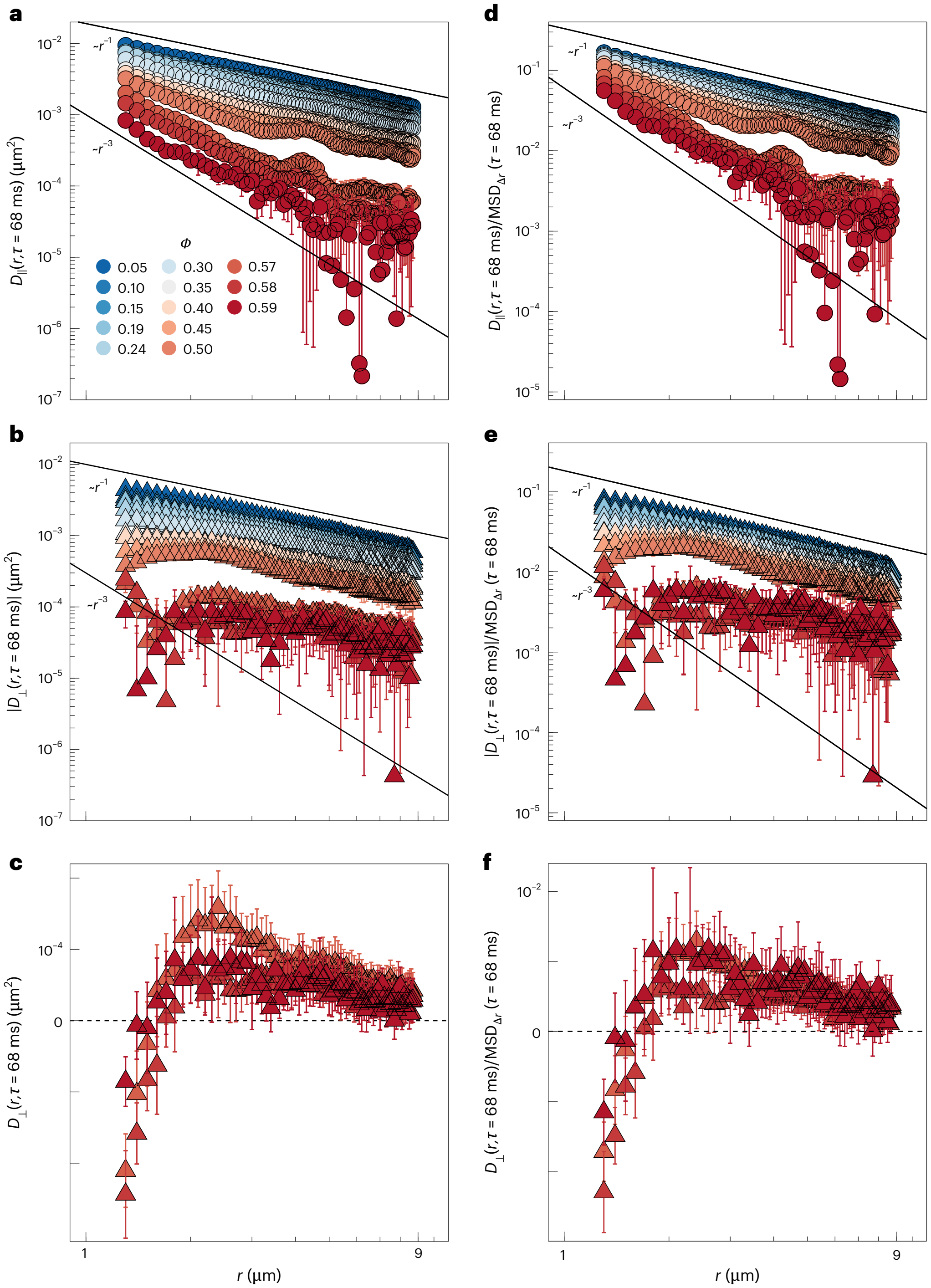

Fig. 4 | The two-point correlations between the tracers' displacements describe the flow of the dispersion medium in-between the matrix particles. **a**–**c**, Longitudinal $D_\parallel(r,\tau)$ (**a**) and transversal $D_\perp(r,\tau)$ (**b** and **c**) correlations for $\tau = 68$ ms and different volume fractions (ϕ) of the colloidal matrix. $D_\parallel(r,\tau)$ is always positive, whereas $D_\perp(r,\tau)$ can be either positive or negative. **b** shows the magnitude of $D_\perp(r,\tau)$ for all values of ϕ, while **c** displays $D_\perp(r,\tau)$ for the three highest-volume fractions, for which a transition from negative to positive transversal correlations is observed. **d**–**f**, The corresponding correlations normalized by the tracers' mean squared displacement $\text{MSD}_{\Delta r}(\tau = 68\text{ ms})$. The solid lines denote the power-law decays as indicated. The data in **a**–**f** represent the weighted mean from N_{area} (≥10) different areas (technical replicates), where N_{area} varied for each ϕ (Supplementary Table 3). The error bars in **a**–**c** represent the corresponding weighted s.d. The weighting is based on the number of two-point displacements and is applied consistently to both the mean and s.d. calculation. The error bars in **d**–**f** represent the propagated uncertainty, determined by applying the Gaussian error propagation formula, assuming uncorrelated input parameters. The error bars may be smaller than the symbol size.

$$D_\parallel(r,\tau) \equiv \langle \Delta x_1 \Delta x_2 \rangle (r,\tau) = 2k_B T \tau\, G_{xx}(r\hat{\mathbf{x}}), \tag{5a}$$

$$D_\perp(r,\tau) \equiv \langle \Delta y_1 \Delta y_2 \rangle (r,\tau) = 2k_B T \tau\, G_{yy}(r\hat{\mathbf{x}}). \tag{5b}$$

In a neat solvent of viscosity η_0 the flow response $G_{\vartheta\beta}$ reduces to the Oseen tensor[42], $G_{\vartheta\beta}(\mathbf{r}) = (8\pi\eta_0 r)^{-1}\left(\delta_{\vartheta\beta} + r_\vartheta r_\beta / r^2\right)$, or, in Fourier space,

$$\tilde{G}_{\vartheta\beta}(\mathbf{q}) = \frac{1}{\eta_0 q^2}\left(\delta_{\vartheta\beta} - \frac{q_\vartheta q_\beta}{q^2}\right). \tag{6}$$

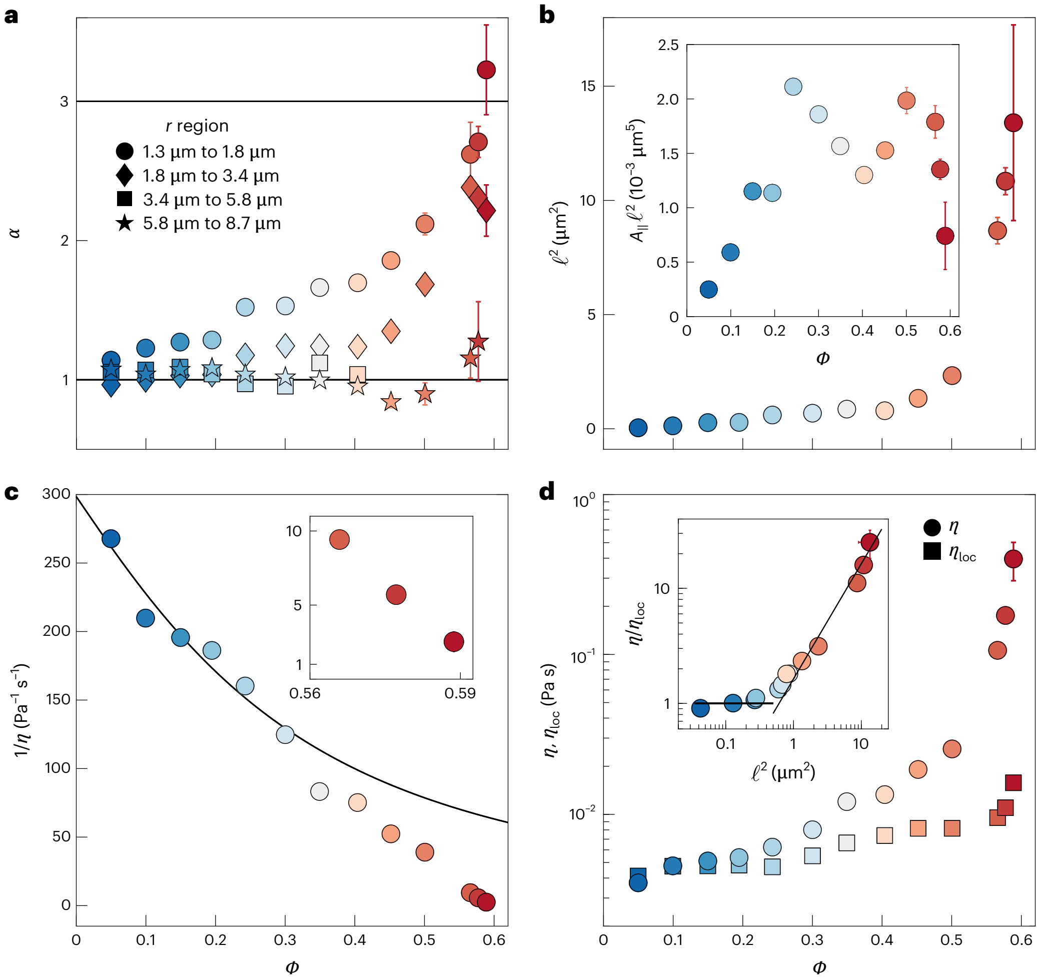

Fig. 5 | Changes in the spatial decay of the longitudinal correlation with increasing volume fraction. **a**, Exponent α of the power-law decay of $D_{\parallel}(r,\tau)$ within different ranges of separation as indicated in the legend. **b**, Crossover length squared obtained from the coefficient of the correlation's r^{-3} term. The inset shows the prefactor $A_{\parallel}\ell^2$ of the r^{-3} term in the correlation function. **c**, Inverse viscosity $1/\eta$ as obtained from the coefficient $A_{\parallel} \propto \eta^{-1}$ of the correlation's r^{-1} term. The solid line shows the low-density theoretical expression known to hold for $\phi \lesssim 0.3$ (ref. 45). The inset focuses on the largest-volume fractions (supercooled suspensions). **d**, Comparison between the viscosity η extracted from the two-tracer correlation and the local viscosity η_{loc} as extracted from the single-tracer mean squared displacement $\mathrm{MSD}_{\Delta r}(\tau = 68\ \mathrm{ms})$. The two viscosities coincide for small ϕ, whereas $\eta \gg \eta_{\mathrm{loc}}$ for large ϕ. The inset shows η/η_{loc} against ℓ^2, exhibiting a roughly linear dependence at large ϕ. For each ϕ, the $D_{\parallel}(r, \tau = 68\ \mathrm{ms})$ and $\mathrm{MSD}_{\Delta r}(\tau = 68\ \mathrm{ms})$ data represent a weighted mean from N_{area} (≥10) different areas (technical replicates), where N_{area} varied (Supplementary Table 3), with the weighting based on the number of displacements (one- or two-point). These $D_{\parallel}(r, \tau = 68\ \mathrm{ms})$ data were fitted using an unweighted nonlinear least-squares algorithm (MATLAB Fitting Toolbox) to determine α (Supplementary Equation 24), and $A_{\parallel}$ and ℓ^2 (Supplementary Equation 26). The error bars for these three parameters represent the 68% confidence interval from the fit. The viscosities η (Supplementary Equation 32) and η_{loc} (Supplementary Equation 34) were calculated. The error bars for η, $1/\eta$, η_{loc}, η/η_{loc} and $A_{\parallel}\ell^2$ represent the propagated uncertainty, determined by applying the Gaussian error propagation formula, assuming uncorrelated input parameters. Error bars may be smaller than the symbol size.

The first factor has a pole at $q = 0$, reflecting the conservation of momentum over large distances[37], while the second factor ensures the conservation of mass (incompressibility), $q_{\beta}\tilde{G}_{\vartheta\beta} = 0$. Thus, as long as a certain fluid is incompressible and conserves momentum, one expects the same expression to hold at sufficiently large r (small q), with merely a change of prefactor $\eta_0 \to \eta$. This rescaled Oseen tensor is used in two-point microrheology[32].

To generalize equation (6) to dispersion media that contain internal structure as in the case of a matrix made of large particles, we consider the following expansion:

$$\tilde{G}_{\vartheta\beta}(\mathbf{q}) = \frac{1}{\eta_0}\frac{1}{A + Bq^2 + Cq^4 + \ldots}\left(\delta_{\vartheta\beta} - \frac{q_{\vartheta}q_{\beta}}{q^2}\right), \qquad (7)$$

where the coefficients A, B and C depend on the matrix's volume fraction ϕ. This expression recovers equation (6) in the limit $B = 1$, $A = C = \ldots = 0$. This modified response is equivalent to a modified Stokes equation containing a term proportional to the velocity (a Brinkman term[43]) and velocity gradients higher than the Laplacian. Another equivalent perspective is to associate with the structured medium a space-dependent viscosity[44], equal to $\eta_0(A/q^2 + B + Cq^2 + \ldots)$, which diverges at $q \to 0$ if $A \neq 0$ (that is, in a solid). We add that one can obtain equation (7) explicitly for a random distribution of spheres, along with explicit expressions for the coefficients in terms of ϕ and the fraction of immobile versus mobile spheres[39]. For example, if all the spheres are mobile, we get $A = 0$ and $B = 1 + (5/2)\phi$, in agreement with Einstein's famous result.

Thus, the effect of the dispersed structure manifests itself as additional poles in the first factor of $\tilde{G}_{\vartheta\beta}(\mathbf{q})$, corresponding to corrections at large, yet progressively smaller, length scales. The incompressibility constraint is enforced by the second factor, which remains unchanged. The only assumptions underlying equation (7) are that the dispersion is rotation- and inversion-symmetric and that the medium is incompressible.

For $A = 0$, the expression in equation (7) has a pole at $q = 0$, and we recover for small q the leading-order behaviour of a momentum-conserving liquid, equation (6), with effective viscosity (global viscosity) $\eta(\phi) = \eta_0 B(\phi)$. For $A \neq 0$, the pole at $q = 0$ is removed, and the medium described by equation (7) does not conserve momentum. Equation (7) then coincides, for small q, with the classical Brinkman theory of flow inside a porous solid[43]. Thus, $A(\phi)$ serves as an 'order parameter' for the colloidal glass transition; it vanishes in the liquid suspension and is non-zero in the solid suspension. Its departure from zero, removing the $q = 0$ pole, marks the breaking of the translation symmetry of the dispersion medium; when pushed, the fluid now flows relative to an overall stationary structure and loses momentum to it.

More specifically, inverting equation (7) from $\mathbf{q}$ to $\mathbf{r}$ and expanding to two leading orders in large r, we obtain

$$\text{liquid}\,(A=0):\quad G_{\vartheta\beta}(\mathbf{r})=\frac{1}{8\pi\eta}\left[\frac{1}{r}\left(\delta_{\vartheta\beta}+\frac{r_\vartheta r_\beta}{r^2}\right)-\frac{\ell^2}{r^3}\left(\delta_{\vartheta\beta}-3\frac{r_\vartheta r_\beta}{r^2}\right)\right],\tag{8a}$$

$$\text{solid}\,(A\neq0):\quad G_{\vartheta\beta}(\mathbf{r})=-\frac{1}{4\pi\eta_0}\frac{\ell_\mathrm{s}^2}{r^3}\left(\delta_{\vartheta\beta}-3\frac{r_\vartheta r_\beta}{r^2}\right),\tag{8b}$$

In addition to the global liquid viscosity $\eta = \eta_0 B$, two dynamic lengths emerge, $\ell = |2C/B|^{1/2}$ and $\ell_\mathrm{s} = A^{-1/2}$, characterizing the liquid and solid suspensions, respectively. Substituting equations (8) in equations (5), we obtain the tracers' displacement correlations,

$$\text{liquid}\,(A=0):\quad D_\parallel(r,\tau)=\frac{k_\mathrm{B}T\tau}{2\pi\eta}\left(\frac{1}{r}+\frac{\ell^2}{r^3}\right),\quad D_\perp(r,\tau)=\frac{k_\mathrm{B}T\tau}{4\pi\eta}\left(\frac{1}{r}-\frac{\ell^2}{r^3}\right)\tag{9a}$$

$$\text{solid}\,(A\neq0):\quad D_\parallel(r,\tau)=\frac{k_\mathrm{B}T\tau}{\pi\eta_0}\frac{\ell_\mathrm{s}^2}{r^3},\qquad D_\perp(r,\tau)=-\frac{k_\mathrm{B}T\tau}{2\pi\eta_0}\frac{\ell_\mathrm{s}^2}{r^3}.\tag{9b}$$

The spatial dependencies of the two-term correlations for a liquid, equation (9a), are shown in Supplementary Fig. 6. Equations (9) are our central predictions. Analysis of the experimental data using equation (9a) confirms its theoretical predictions. First, we note the crossover between the r^{-3} and r^{-1} terms in the correlations, as fitted above. Second, the positive and negative values for the coefficient of the r^{-3} term in $D_\parallel$ and $D_\perp$, respectively, are observed (Fig. 4 and Supplementary Table 5).

Third, the viscosity $\eta(\phi)$ is extracted from the prefactor of the r^{-1} term in the correlations according to equation (9a) (Fig. 5c). The values obtained on the basis of $D_\parallel$ and $D_\perp$ are consistent (Supplementary Information). At low-to-moderate volume fractions ($\phi \lesssim 0.3$) the measured viscosities (Fig. 5c) are reasonably in agreement with the known low-density expression[45]. This confirms that the tracers reliably reproduce the global viscosity of the suspension over the measurement time.

Figure 5b shows a steep increase of $\ell^2(\phi)$ with ϕ in the supercooled range. As a result, the r^{-3} correlation term becomes more important compared with the term r^{-1}, leading to the observed increase of the exponent α with ϕ (Fig. 5a). Unlike the prefactor of the term r^{-1}, $A_\parallel \propto \eta^{-1}$, the prefactor of the term r^{-3}, $A_\parallel \ell^2 \propto \ell^2/\eta$, is found to depend much more weakly on ϕ (Fig. 5b, inset, and Supplementary Table 5). This binds the increase of ℓ with that of the viscosity according to $\ell(\phi) \propto \eta(\phi)^{1/2}$. Thus, if the viscosity diverges at the glass transition, so must the length ℓ. A way to interpret this observation is that the mechanism underlying the r^{-3} term depends on the local viscosity experienced by the small tracers, η_loc (which should have a weak dependence on ϕ), and not on the sharply increasing global viscosity of the suspension, η (refs. 36,37). To check this, we extract $\eta_\mathrm{loc}(\phi)$ from the observed mean square displacement $\mathrm{MSD}_{\Delta r}(\tau)$ of a single tracer according to the Stokes–Einstein relation, $\mathrm{MSD}_{\Delta r}(\tau) = 2k_\mathrm{B}T\tau/(3\pi\eta_\mathrm{loc}a_\mathrm{s})$ (Supplementary Information). The results are shown, along with the global viscosity $\eta(\phi)$, in Fig. 5d. Although the two viscosities coincide in the dilute suspensions, they substantially differ at larger ϕ, with η increasing sharply and η_loc only moderately. As anticipated by the conjecture $A_\parallel \sim \ell^2/\eta \sim 1/\eta_\mathrm{loc}$, for these large-volume fractions, the ratio η/η_loc is found to be roughly proportional to ℓ^2 (Fig. 5d, inset).

Conclusion

We have exploited random thermal flows in a dispersion medium, captured by displacement correlations between tracers, to gain insight into the dynamic arrest of colloidal suspensions. This indirect approach yields new observables that mirror the approaching glass transition and are based on strong signals that can be experimentally measured. We highlighted three observables: the transversal correlation $D_\perp(r,\tau)$, the crossover length ℓ between the two leading contributions to $D_\parallel(r,\tau)$ or $D_\perp(r,\tau)$, and the power-law exponent α of the decay of $D_\parallel(r,\tau)$ and $D_\perp(r,\tau)$. $D_\perp(r,\tau)$ develops a distinctive negative contribution that becomes increasingly dominant towards the glass transition (Fig. 4b,c and equation (9a)). Beyond the glass transition, this contribution should completely dominate the large-separation transversal correlation (equation (9b)). As the glass transition is approached, $\ell(\phi)$ and the corresponding viscosity $\eta(\phi)$ steeply increase together, as $\ell \propto \eta^{1/2}$ (Fig. 5). This is in line with a recent report on the power-law increase of a differently defined structural length in colloidal suspensions with the relaxation time, having an exponent of approximately 0.54 (ref. 46). The connection between ℓ and η established here ($\ell(\phi) \propto \eta(\phi)^{1/2}$) implies that ℓ must diverge at the glass transition. Finally, the decay exponent α changes at the glass transition from $\alpha = 1$, characteristic of a liquid, to $\alpha = 3$, indicating a solid (Fig. 5a and equations (9)). We have tied this observation to the breaking of translation symmetry of the dispersion medium. The experimental observations can thus be rationalized on the basis of conservation laws without resorting to a specific model. The price of such a generic approach is that the predictions depend on phenomenological parameters (A, B and C) to be determined by different methods. Our experimental method also reveals subtle spatial features of the approach to the glass transition. As long as ℓ is finite, the correlations consist of a mixture of two terms, leading to 'solid-like' correlations ($\propto r^{-3}$) for $r < \ell$ mixed with 'liquid-like' correlations ($\propto r^{-1}$) for $r > \ell$ (equation (9a) and the corresponding fits of the data in Fig. 4a,b). This resembles the situation in continuous phase transitions. Only when the measurements cover asymptotically large distances $r \gg \ell$ will the changes in the symmetry-determined power α and the large separation sign of $D_\perp$ be sharply located at the transition.

The spatial dependence of the pair correlations raises a question concerning the glassiness of the suspensions with $\phi \geq 0.58$. If our measurements were restricted to $r \lesssim 2\,\mu\mathrm{m}$, we would find for these suspensions a negative $D_\perp$ (Fig. 4c) and $\alpha = 3$ (Fig. 5a) and conclude that the suspensions were solid. This would agree with the common view of the location of colloidal glass transition for hard spheres[20]. Indeed, the displacement fluctuations of single large particles show caging at these high-volume fractions (Fig. 2c). However, once the measurements are extended to larger distances, liquid-like behaviour ($\alpha \approx 1$ and positive $D_\perp$) is found even for $\phi \geq 0.58$. This is particularly evident from the asymptotic decay of $D_\perp$ to zero from positive values (Fig. 4c). The same holds quite clearly, albeit less robustly, for $\phi = 0.60$ as shown in Supplementary Fig. 19. Indeed, we have extracted finite values of η and ℓ for these suspensions (Fig. 5b,c). Thus, the new signatures presented here indicate that the colloidal glass transition for hard spheres occurs at larger volume fractions than usually expected. This finding is in line with ref. 47, which reported fluid behaviour up to a volume fraction of 0.597 using dynamic light scattering. While the finding of ref. 47 required measurements over 10^3 s, ours has been obtained over 68 ms. The volume fraction at which the large-scale liquid behaviour completely disappears and the suspension can be considered solid on all scales remains unclear. The data for $1/\eta$ (Fig. 5c, inset) does not preclude the possibility that this might occur only at random close packing ($\phi_{\mathrm{RCP}} \approx 0.64$).

We also leave two interesting aspects for future investigation. What does the observed scaling between the crossover length and the relaxation time, $\ell(\phi) \propto \tau_{\mathrm{r}}(\phi)^{1/2}$, imply about the properties of the domains of cooperatively moving particles associated with ℓ (refs. 3,48)? How does the characteristic length in the solid, ℓ_{s} (equation (9b)), change as the glass transition is approached from the solid side? The weaker correlations between the tracers in the glass would require particularly accurate measurements to answer the last question. A growing ℓ_{s} (ref. 39), if found, might be associated with the growth of plastic 'soft spots' proposed to accompany glass melting[49].

Finally, the experimental method presented here can be applied to any other system that includes a dispersion medium, for example, polymer solutions that, upon cross-linking or entanglement, solidify into a gel[50], or dispersed fibre networks that undergo a rigidity transition in response to applied shear[51]. Relevant systems also include biological samples, such as actin networks[52] and cells or groups of cells, for which the concept of glassiness is gaining increasing relevance.

Online content

Any methods, additional references, Nature Portfolio reporting summaries, source data, extended data, supplementary information, acknowledgements, peer review information; details of author contributions and competing interests; and statements of data and code availability are available at https://doi.org/10.1038/s41567-025-03140-z.

References

1. Berthier, L., Biroli, G., Bouchaud, J.-P., Cipelletti, L. & Saarloos, W. *Dynamical Heterogeneities in Glasses, Colloids, and Granular Media* (Oxford Univ. Press, 2011).
2. Wolynes, P. G. & Lubchenko, V. *Structural Glasses and Supercooled Liquids: Theory, Experiment, and Applications* (Wiley, Hoboken, 2012).
3. Weeks, E. R., Crocker, J. C., Levitt, A. C., Schoefield, A. & Weitz, D. A. Three-dimensional direct imaging of structural relaxation near the colloidal glass transition. *Science* **287**, 627–631 (2000).
4. Karmakar, S., Lerner, E. & Procaccia, I. Direct estimate of the static length-scale accompanying the glass transition. *Physica A* **391**, 1001–1008 (2012).
5. Tanaka, H., Kawasaki, T., Shintani, H. & Watanabe, K. Critical-like behaviour of glass-forming liquids. *Nat. Mater.* **9**, 324–331 (2010).
6. Parisi, G. & Zamponi, F. Mean-field theory of hard sphere glasses and jamming. *Rev. Mod. Phys.* **82**, 789–845 (2010).
7. Biroli, G. & Bouchaud, J.-P. in *Structural Glasses and Supercooled Liquids: Theory, Experiment, and Applications* (eds Wolynes, P. G. & Lubchenko, V.) Ch. 2 (Wiley, 2012).
8. Dauchot, O., Ladieu, F. & Royall, C. P. The glass transition in molecules, colloids and grains: universality and specificity. *C. R. Phys.* **24**, 25–56 (2023).
9. Wang, W. H. Bulk metallic glasses with functional physical properties. *Adv. Mater.* **21**, 4524–4544 (2009).
10. Zhou, E. H. et al. Universal behavior of the osmotically compressed cell and its analogy to the colloidal glass transition. *Proc. Natl Acad. Sci. USA* **106**, 10632–10637 (2009).
11. Sadati, M., Nourhani, A., Fredberg, J. J. & Qazvini, N. T. Glass-like dynamics in the cell and in cellular collectives. *Wiley Interdiscip. Rev. Syst. Biol. Med.* **6**, 137–149 (2014).
12. Angelini, T. E. et al. Glass-like dynamics of collective cell migration. *Proc. Natl Acad. Sci. USA* **108**, 4714 (2011).
13. Park, J.-A. et al. Unjamming and cell shape in the asthmatic airway epithelium. *Nat. Mater.* **14**, 1040–1048 (2015).
14. Bi, D., Lopez, J. H., Schwarz, J. M. & Manning, M. L. A density-independent rigidity transition in biological tissues. *Nat. Phys.* **11**, 1074–1077 (2015).
15. Bi, D., Yang, X., Marchetti, M. C. & Manning, M. L. Motility-driven glass and jamming transitions in biological tissues. *Phys. Rev. X* **6**, 021011 (2016).
16. Chepizhko, O. et al. Bursts of activity in collective cell migration. *Proc. Natl Acad. Sci. USA* **113**, 11408–11413 (2016).
17. Mongera, A. et al. A fluid-to-solid jamming transition underlies vertebrate body axis elongation. *Nature* **561**, 401–405 (2018).
18. Atia, L. et al. Geometric constraints during epithelial jamming. *Nat. Phys.* **14**, 613–620 (2018).
19. Grosser, S. et al. Cell and nucleus shape as an indicator of tissue fluidity in carcinoma. *Phys. Rev. X* **11**, 011033 (2021).
20. Hunter, G. L. & Weeks, E. R. The physics of the colloidal glass transition. *Rep. Prog. Phys.* **75**, 066501 (2012).
21. Gokhale, S., Sood, A. K. & Ganapathy, R. Deconstructing the glass transition through critical experiments on colloids. *Adv. Phys.* **65**, 363–452 (2016).
22. Pusey, P. N. & Megen, W. Phase behaviour of concentrated suspensions of nearly hard colloidal spheres. *Nature* **320**, 340–342 (1986).
23. Pusey, P. N. in *Liquides, Cristallisation et Transition Vitreuse/ Liquids, Freezing and Glass Transition* (eds Hansen, J. P. et al.) 763–942 (Elsevier Science Publishers B.V., 1991).
24. Cheng, Z. et al. Phase diagram of hard spheres. *Mater. Des.* **22**, 529–534 (2001).
25. Royall, C. P., Poon, W. C. K. & Weeks, E. R. In search of colloidal hard spheres. *Soft Matter* **9**, 17 (2013).
26. Sentjabrskaja, T. et al. Anomalous dynamics of intruders in a crowded environment of mobile obstacles. *Nat. Commun.* **7**, 11133 (2016).
27. Sentjabrskaja, T. et al. Binary colloidal glasses: linear viscoelasticity and its link to the microscopic structure and dynamics. *Soft Matter* **15**, 2232–2244 (2019).
28. Lázaro-Lázaro, E. et al. Glassy dynamics in asymmetric binary mixtures of hard spheres. *Phys. Rev. E* **99**, 042603 (2019).
29. Zhang, R. & Schweizer, K. S. Correlated matrix-fluctuation-mediated activated transport of dilute penetrants in glass-forming liquids and suspensions. *J. Chem. Phys.* **146**, 194906 (2017).
30. Laurati, M., Sentjabrskaja, T., Ruiz-Franco, J., Egelhaaf, S. U. & Zaccarelli, E. Different scenarios of dynamic coupling in glassy colloidal mixtures. *Phys. Chem. Chem. Phys.* **20**, 18630–18638 (2018).
31. Poling-Skutvik, R. et al. Structure dominates localization of tracers within aging nanoparticle glasses. *J. Phys. Chem. Lett.* **10**, 1784–1789 (2019).
32. Crocker, J. C. et al. Two-point microrheology of inhomogeneous soft materials. *Phys. Rev. Lett.* **85**, 888–891 (2000).
33. Yethiraj, A. & Blaaderen, A. A colloidal model system with an interaction tunable from hard sphere to soft and dipolar. *Nature* **421**, 513–517 (2003).
34. Diamant, H., Cui, B., Lin, B. & Rice, S. A. Correlated particle dynamics in concentrated quasi-two-dimensional suspensions. *J. Phys. Condens. Matter* **17**, S4047 (2005).
35. Prasad, V., Koehler, S. A. & Weeks, E. R. Two-particle microrheology of quasi-2D viscous systems. *Phys. Rev. Lett.* **97**, 176001 (2006).
36. Diamant, H. Long-range hydrodynamic response of particulate liquids and liquid-laden solids. *Isr. J. Chem.* **47**, 225–231 (2007).
37. Diamant, H. Hydrodynamic interaction in confined geometries. *J. Phys. Soc. Jpn* **78**, 041002 (2009).

38. Crocker, J. C. Measurement of the hydrodynamic corrections to the Brownian motion of two colloidal spheres. *J. Chem. Phys.* **106**, 2837–2840 (1997).
39. Diamant, H. Model-free hydrodynamic theory of the colloidal glass transition. Preprint at https://arxiv.org/abs/2411.06270 (2024).
40. Ermak, D. L. & McCammon, J. A. Brownian dynamics with hydrodynamic interactions. *J. Chem. Phys.* **69**, 1352–1360 (1978).
41. Brady, J. F. & Bossis, G. Stokesian dynamics. *Annu. Rev. Fluid Mech.* **20**, 111–157 (1988).
42. Kim, S. & Karrila, S. J. *Microhydrodynamics: Principles and Selected Applications* (Dover Publications, 2005).
43. Brinkman, H. C. A calculation of the viscous force exerted by a flowing fluid on a dense swarm of particles. *Appl. Sci. Res.* **A1**, 27–34 (1947).
44. Grosberg, A. Y., Joanny, J.-F., Srinin, W. & Rabin, Y. Scale-dependent viscosity in polymer fluids. *J. Phys. Chem. B* **26**, 6383–6390 (2016).
45. Batchelor, G. K. The effect of Brownian motion on the bulk stress in a suspension of spherical particles. *J. Fluid Mech.* **83**, 97–117 (1977).
46. Hu, J., Ning, L., Liu, R., Yang, M. & Chen, K. Evidence for growing structural correlation length in colloidal supercooled liquids. *Phys. Rev. E* **106**, 054601 (2022).
47. Brambilla, G. et al. Probing the equilibrium dynamics of colloidal hard spheres above the mode-coupling glass transition. *Phys. Rev. Lett.* **102**, 085703 (2009).
48. Diamant, H. Criteria of amorphous solidification. Preprint at https://arxiv.org/abs/1406.2508 (2014).
49. Aharonov, E. et al. Direct identification of the glass transition: growing length scale and the onset of plasticity. *Europhys. Lett.* **77**, 56002 (2007).
50. Rubinstein, M. & Colby, R. H. *Polymer Physics* (Oxford Univ. Press, 2003).
51. Licup, A. J. et al. Stress controls the mechanics of collagen networks. *Proc. Natl Acad. Sci. USA* **112**, 9573–9578 (2015).
52. Sonn-Segev, A., Bernheim-Groswasser, A., Diamant, H. & Roichman, Y. Viscoelastic response of a complex fluid at intermediate distances. *Phys. Rev. Lett.* **112**, 088301 (2014).

Methods

Sample

We studied binary mixtures of PMMA colloidal spheres. The particles were fluorescently labelled with monomerized rhodamine B (small particles) or NBD (large particles) and sterically stabilized with poly(12-hydroxy-stearic acid) by covalently binding the stabilizer to the surface of the particles[53]. The small particles (tracers) had a diameter $2a_\mathrm{s} = (0.50 \pm 0.02)$ µm and a polydispersity $\delta_\mathrm{s} \approx 7\%$ and the large (matrix) particles had a diameter $2a_\mathrm{l} = (3.19 \pm 0.02)$ µm and a polydispersity $\delta_\mathrm{l} \approx 7\%$ as determined using confocal differential dynamic microscopy[54]. The particles are suspended in an index- and density-matched mixture of *cis*-decalin and cycloheptylbromide that prevents particle sedimentation and turbidity. The suspension also behaves as a hard-sphere-like system[23,25,33], where interactions between particles occur only upon contact. Assuming that the sediments were randomly close-packed with a volume fraction $\phi_\mathrm{RCP} = 0.65$ (ref. 55), binary suspensions with a volume fraction of large particles $0.050 \lesssim \phi \lesssim 0.601$ and of small particles $0.005 \lesssim \phi_\mathrm{s} \lesssim 0.008$ were prepared. The statistical uncertainty of the ratios of volume fractions is expected to be smaller than 10^{-4}, in agreement with previous reports[56]. Details about the sample preparation can be found in Supplementary Section 1.1 and the samples studied in Supplementary Table 1.

Sample cell

The sample cells were built from a microscope slide with an area of 76 × 26 mm^2, a thickness of 1 mm (631-1550, vwr), a cover glass with an area of 20 × 20 mm^2 and a thickness between 0.13 mm and 0.16 mm (Nr. 1, 631-1568, vwr). In the centre of the microscope slide, a cylindrical cavity with a diameter of approximately 3 mm and a depth of approximately 0.5 mm was drilled. The cylindrical cavity in a cleaned microscope slide was filled with the sample using either a stainless-steel spatula or a micropipette with a cut pipette tip to avoid self-filtration effects[57]. Then, a cleaned cover glass was placed on the cavity. The sample was sealed with glue (All Purpose Adhesive Super, UHU). The glue was left to dry for at least 12 h while the cell was rotated to homogenize the contained sample. Details about the cleaning process are given in Supplementary Section 1.2.

Confocal microscopy

The samples were imaged using a confocal scanning unit (A1R-MP, Nikon) mounted on an inverted microscope (Eclipse Ti, Nikon) with a 60× oil immersion objective with a numerical aperture of 1.4 (Plan Apo VC, MRD01602, Nikon). Solid-state lasers with wavelengths of 561 nm and 488 nm were used to excite the rhodamine B and NBD fluorescence dyes from the small and large particles, respectively.

Without 3D scan, time series of images with 512 × 512 pixels, usually with an optical section of 0.42 µm and a pixel pitch of 0.105 µm per pixel, were recorded at a fixed distance of 30–60 µm from the cover glass. More details are given in Supplementary Section 1.3 and Supplementary Table 2.

Analysis procedure

A series of time-lapse microscopy images was used to extract the 2D trajectories $\mathbf{R}_i(t)$ of the matrix (large) and $\mathbf{r}_{i,a}(t)$ of the tracer (small) particles, using i as particle ID, a as area (field of view) and t as starting time. Trajectories that complied with a specified trajectory length were used to determine one-point observables such as the MSD.

To ensure consistent dynamics from all the different areas (measurements) of the tracer particles, we performed an equilibration check of the variances $\sigma^2_{\Delta r_a}(\tau)$ ($\mathrm{MSD}_{\Delta r}$), with τ as the delay time. We considered an area a as equilibrated when $\sigma^2_{\Delta r_a}(\tau)$ presented dynamical information equivalent to the ones with the largest time span after filling the sample in the sample cell. All one-point observables from equilibrated areas a were then averaged.

The corresponding trajectories that passed the equilibration check were used to determine the two-point correlation functions $D_\parallel(r,\tau)$ and $D_\perp(r,\tau)$ for a specific τ and distances r between the tracer particles. We first fitted the two-point correlation functions to determine the decay exponents $\alpha_\parallel$ (α) and $\alpha_\perp$ for different r regions. In a subsequent fitting process, we used an analytical expression for the two-term correlations to extract the prefactors $A_\parallel$, $A_\perp$ and the crossover lengths squared $\ell_\parallel^2$ (ℓ^2) and $\ell_\perp^2$. We performed a consistency check by fitting this same expression to a calculated analytical form using the extracted quantities. Finally, we used the Stokes–Einstein relation to determine the local viscosity η_loc and determined the global viscosities $\eta_\parallel$ (η) and $\eta_\perp$ from the prefactors $A_\parallel$ and $A_\perp$, respectively. Details are given in Supplementary Section 2.

Data availability

The data that support the findings of this study are available via Zenodo at https://doi.org/10.5281/zenodo.17533166 (ref. 58) in MATLAB data file format.

Code availability

The MATLAB codes used for the analysis in this study are available via Zenodo at https://doi.org/10.5281/zenodo.17533166 (ref. 58).

References

53. Antl, L. et al. The preparation of poly(methyl methacrylate) latices in non-aqueous media. *Colloids Surf.* **17**, 67–78 (1986).
54. Giavazzi, F., Edera, P., Lu, P. J. & Cerbino, R. Image windowing mitigates edge effects in differential dynamic microscopy. *Eur. Phys. J. E* **40**, 97 (2017).
55. Schaertl, W. & Sillescu, H. Brownian dynamics of polydisperse colloidal hard spheres: equilibrium structures and random close packings. *J. Stat. Phys.* **77**, 1007–1025 (1994).
56. Poon, W. C. K., Weeks, E. R. & Royall, C. P. On measuring colloidal volume fractions. *Soft Matter* **8**, 21–30 (2012).
57. Haw, M. D. Jamming, two-fluid behavior, and 'self-filtration' in concentrated particulate suspensions. *Phys. Rev. Lett.* **92**, 185506 (2004).
58. Escobedo Sanchez, M. A. & Laerman, P. Emergent signatures of the glass transition codes. *Zenodo* https://doi.org/10.5281/zenodo.17533166 (2025).

Acknowledgements

This work was supported by the German-Israeli Foundation for Scientific Research & Development (GIF), research grant no. I-1345-303.10-2016. H.D., M.A.E.S., P.L., S.U.E. and Y.R. were supported by this grant.

Author contributions

Author initials are listed alphabetically within each contribution role. Conceptualization: H.D., S.U.E. and Y.R. Data curation: M.A.E.S. and P.L. Formal analysis: H.D., P.L. and Y.R. Funding acquisition: H.D. and S.U.E. Investigation: M.A.E.S. and P.L. Methodology: H.D. and Y.R. Project administration: S.U.E. Resources: S.U.E. Software: M.A.E.S., P.L. and Y.R. Supervision: M.A.E.S. and S.U.E. Validation: H.D., I.B., M.A.E.S., P.L., S.U.E. and Y.R. Visualization: P.L. and S.U.E. Writing—original draft: H.D. and S.U.E. Writing—review and editing: H.D., I.B., M.A.E.S., P.L., S.U.E. and Y.R.

Funding

Open access funding provided by Heinrich-Heine-Universität Düsseldorf.

Competing interests

The authors declare no competing interests.

Additional information

Supplementary information The online version contains supplementary material available at https://doi.org/10.1038/s41567-025-03140-z.

Correspondence and requests for materials should be addressed to Manuel A. Escobedo-Sánchez.

Peer review information *Nature Physics* thanks Andreas Neophytou and the other, anonymous, reviewer(s) for their contribution to the peer review of this work.